Propagation of fluid-driven aseismic slip fronts along crustal faults

François Passelègue

francois.passelegue@cnrs.fr

CNRS

Nicolas Brantut

GFZ Helmholtz-Zentrum

Hervé Chauris

Mines de Paris

Pierre Dublanchet

Mines de Paris

Physical Sciences - Article

Keywords:

Posted Date: June 4th, 2025

DOI: https://doi.org/10.21203/rs.3.rs-6812099/v1

Additional Declarations: There is **NO** Competing Interest.

Propagation of fluid-driven aseismic slip fronts along crustal faults

François Passelègue[1,*+], Nicolas Brantut[2,3,+], Hervé Chauris[4], and Pierre Dublanchet[4]

[1]Université Côte d'Azur, CNRS, Observatoire de la Côte d'Azur, IRD, Géoazur, Sophia Antipolis, France.
[2]Department of Earth Sciences, University College London, London, UK.
[3]GFZ Helmholtz Centre for Geosciences, Potsdam, Germany.
[4]Mines Paris, PSL University, Centre for geosciences and geoengineering, Fontainebleau, France.
[*]francois.passelegue@cnrs.fr
[+]these authors contributed equally to this work

ABSTRACT

Fluid-induced seismicity results from complex interactions between fluid injection, fault friction, and the ambient stress field. While seismic swarms often display spatiotemporal migration[1–6], it remains unclear whether this reflects fluid pressure diffusion or stress transfer from aseismic slip[7–9]. Fracture mechanics models suggest that aseismic slip may either lag behind or outpace the fluid pressure front, depending on injection conditions and the fault's initial stress state[10–12]. However, direct experimental validation of these predictions has been lacking[10,13]. Here, we report laboratory experiments on granite samples under upper crustal stress conditions[14,15], where we simultaneously tracked the propagation of fluid pressure and aseismic slip during fluid injection[16]. We show that aseismic slip lags the pressure front at low injection rates and low initial stress, but rapidly outpaces it under high-rate injection or near-failure initial stress conditions. The transition is governed by a dimensionless loading parameter that integrates injection rate, fault strength, and initial shear stress. Our results provide direct support for fracture mechanics models of fluid-induced aseismic slip[10–12] and suggest that in critically stressed crustal faults, rupture propagation may commonly outpace fluid diffusion. These findings help reconcile contrasting observations of seismicity migration[7–9] and improve our understanding of induced seismic hazards[17–20].

Introduction

Understanding the propagation of fluid-driven frictional ruptures is crucial for assessing the hazard of fluid-induced seismicity, whether arising from natural processes[3,4] or human activities[17–20]. These ruptures are often inferred from seismicity along natural faults[1,2,5,6,9] or near anthropogenic fluid injection sites[7,17,21,22]. In cases of induced seismicity, it is well established that the injected fluid volume primarily controls the cumulative aseismic moment[23] and can influence the maximum magnitude of induced earthquakes[24,25].

Seismological observations indicate that seismicity migration often follows a square-root dependence on time, consistent with fluid diffusion along a fault plane. However, this pattern is not universal; in some cases, seismicity propagates linearly with time, suggesting alternative mechanisms such as stress transfer or aseismic slip[7,8]. Moreover, hydraulic diffusivity estimates derived from seismicity migration are typically one to two orders of magnitude larger than those observed in laboratory experiments and natural rock formations[26,27]. This discrepancy may be explained by the fact that, under certain conditions, seismicity is linked to a fluid-driven aseismic slip front, R, that also grows as $\sqrt{t}$[10,12]. The existence of propagating aseismic slip results in a complex and non-systematic relationship between seismicity patterns and the propagation of the fluid pressure front, L. The interplay between the slip and fluid fronts introduces significant variability in seismic responses, complicating efforts to generalize the spatiotemporal evolution of induced seismicity.

A key question remains: under what conditions is induced seismicity primarily governed by the propagation of the fluid pressure front, L, versus an aseismic slip front, R, which may be driven by L but can either lag behind or outpace it? Recent theoretical studies suggest that the transition between these two end-member cases is governed by a loading parameter, T, which depends on the initial stress state of the fault and the magnitude of the pore pressure change[10–12]. However, experimental validation or field observations to test this hypothesis remain lacking. On the one hand, the absence of continuous, in situ measurements of active fault deformation and hydrological processes limit our understanding of fluid-activated aseismic slip, which currently relies on indirect observations such as seismicity migration[4,5,9] or surface geodetic data[3]. On the other hand, measuring both R and L along a limited-sized experimental fault remains challenging[13,14,28], as it does during in situ fluid injection experiments along shallow aseismic faults[29,30], where estimates of the initial state of stress are also lacking. Determining the key parameters controlling the growth of injection-induced ruptures is critical for improving predictive models

of induced seismicity, particularly in applications such as geothermal energy production, wastewater disposal, and carbon sequestration.

Here, we address this question by conducting laboratory experiments where the fluid pressure front, L, and the aseismic slip front, R, can be tracked directly under controlled stress conditions. Our experiments suggest that the question of whether fluid-induced aseismic slip lags behind or outpaces fluid migration is governed primarily by the loading parameter identified in earlier theoretical work[10,12], suitably modified to account for the injection scenario.

Results

The experimental fault consists of a saw-cut granite specimen, oriented at an angle θ of 30° with respect to the principal stress σ_1. Fluid injection was carried out under varying stress conditions through a borehole that directly connects a high-pressure fluid reservoir to the fault plane at its top edge. A second borehole, located on the opposite side of the fault, was used to monitor pore pressure changes (Figure 1a). Additionally, three individual pore pressure sensors were positioned at different locations along the fault in order to track the spatiotemporal evolution of fluid pressure during injection[31,32].

To complement fluid pressure measurements, an array of eight strain gauges was placed around the fault to monitor changes in axial strain (Figure 1a). This array was used to detect the location of the aseismic slip front during fluid injection[16].

The experiments were carried out under stress relaxation conditions[14,27] (see Methods) at an initial (Terzaghi) effective confining pressure of $\sigma_3' = 70$ MPa. Prior to injection, we probed the frictional strength τ_p of the fault by loading the sample at constant rate until slip was detected. In a first stage, the differential stress $(\sigma_1' - \sigma_3')$ was increased to reach a value of initial shear stress $\tau_0 = (\sigma_1' - \sigma_3')\sin(2\theta)/2$ equal to 60% of the fault strength. Injections were then carried out at constant pressure rates c of 0.15, 1.5, and 15 MPa/s, until the complete release of differential stress. In a second stage, the differential stress was raised to 90% of the fault strength. Under these conditions, four different constant pressure rates c were tested: 0.015, 0.15, 1.5, and 15 MPa/s (see Supplementary Table S1). Note that the fluid pressure rates were imposed constant up to a maximum value of 70 MPa ($\sigma_3' = 10$ MPa). If fault reactivation did not occur at this target value, the fluid pressure was kept constant until the complete release of differential stress. This case only occured for the maximum injection rate tested (c=15 MPa/s).

We present typical mechanical data recorded at $\tau_0/\tau_p = 0.6$ for injection rates of $c = 0.15$ MPa/s and $c = 15$ MPa/s in Figure 1. At low injection rates, the fluid pressure increase at the injection site leads to a gradual rise in fluid pressure detected across all pore pressure sensors before the onset of macroscopic slip (Figure 1b). At any given time, the pressure measured at each sensor decreases with increasing distance from the injection site, indicating the propagation of a fluid pressure "front" along the fault. The evolution of axial strain recorded by the strain gauges reveals that strain release initiates earlier near the injection site and later at locations farther along the fault (Figure 1c), indicating the occurrence of slip propagation. Once strain release initiates on all strain gauges, macroscopic fault slip is recorded by the external displacement transducer, and a drop in shear stress is measured with the external load cell. This reduction in shear stress mirrors the evolution of slip along the fault up to the end of the injection phase (Figure 1b), in agreement with the stress relaxation condition imposed by the fixed piston position.

At higher injection rates, only the sensor that is closest to the injection site records an increase in fluid pressure before slip onset (Figure 1d). In addition, deviations from linearity on the strain gauges propagate faster than at $c = 0.15$ MPa/s (Figure 1e). Once the macroscopic slip begins, the release of stress also mirrors of the slip occurring along the fault, as observed at low injection rates.

Inversion of the slip front velocity and of the fluid pressure front

To further analyze the interaction between the slip front and the fluid pressure front, we performed two inversion procedures using the strain gauge and the fluid pressure sensor arrays distributed around the fault (Figure 1a).

Firstly, for each injection, we manually identified the first abrupt release of strain on each strain gauge located around the fault (Figure 1c and 1e). This strain release is expected to indicate the passage of the slip front across the strain gauges, as suggested by synthetic crack propagation using the Green's functions[33] of our fault system (see Methods and Extended Data S1). Next, we performed an inversion to determine the best solution for the slip front velocity ($\dot{R}$), the nucleation location, and the propagation initiation time, assuming a simplified circular front propagation. The minimization of the difference between the experimental and theoretical arrival times provided the optimal solution for these three parameters. In each injection, the slip front nucleates in the area surrounding the injection site (Extended Data S2a). Increasing injection rate leads to an increase in rupture front velocity (Extended Data S2b-h). In addition, a high background stress level also seems to enhance $\dot{R}$. For a similar pressurisation rate, the slip front propagates faster at $\tau_0/\tau_p = 0.9$ than at $\tau_0/\tau_p = 0.6$.

Secondly, we performed an inversion to reconstruct the fluid pressure distribution along the fault during each injection. To account for dead-volume effects in the pore pressure system, we constrained the inversion by imposing the fluid pressure at the injection site (P_1) and the pore pressure measured in the second borehole (P_5). We then inverted for hydraulic diffusivity in both time and space, assuming three independent regions, each monitored by an individual fluid pressure transducer (P_2, P_3, and P_4).

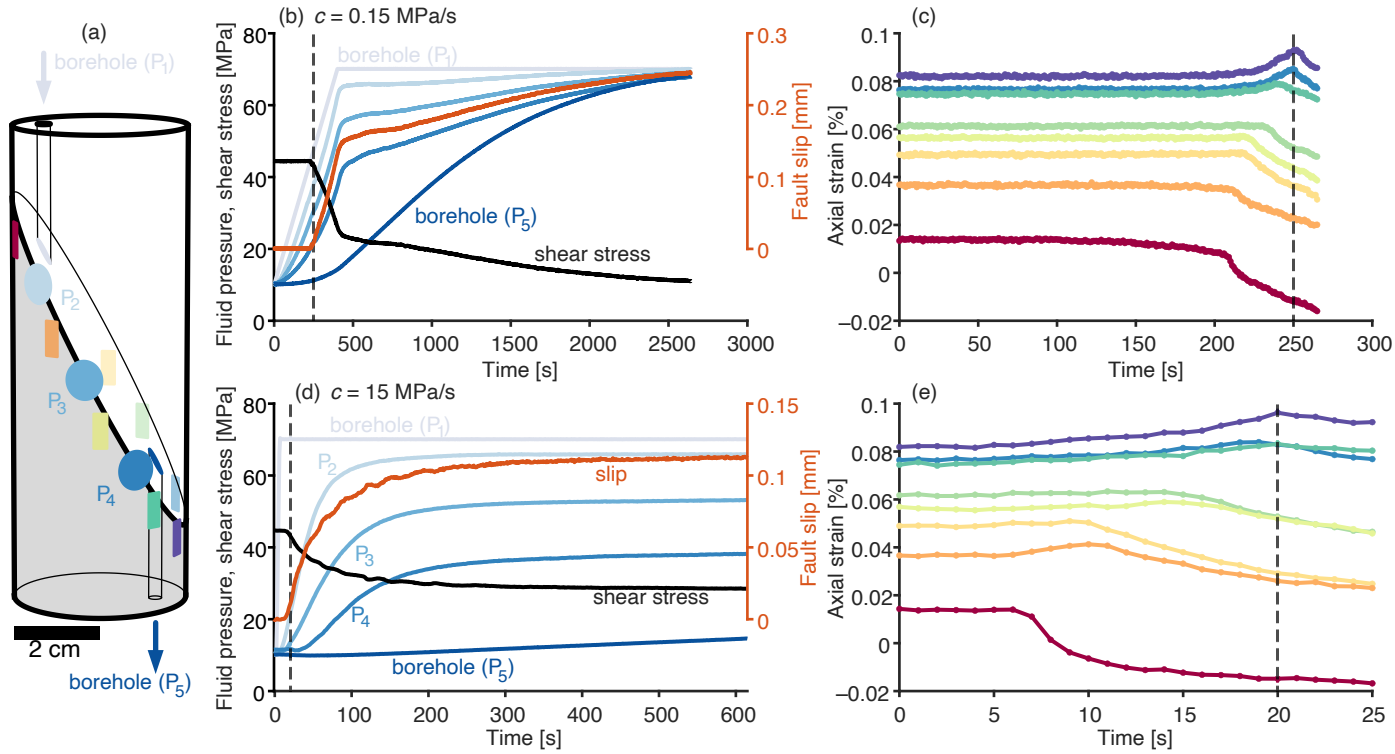

Figure 1. Experimental methods. a. Schematic representation of the sample assembly used in this study. The host rock is Westerly Granite. Rectangles indicate the location of strain gauges around the fault. The injection borehole and the measurement borehole correspond to pressures P_1 and P_5, respectively. **b.** Evolution of macroscopic shear stress, macroscopic fault slip, and fluid pressure measured at five different locations (colors correspond to those shown in **a**) during an injection performed at $\tau_0/\tau_p = 0.6$, with a constant pressure rate of $c = 0.15$ MPa/s. **c.** Evolution of axial strain recorded by the strain gauge array before the onset of macroscopic slip, indicated by the dashed line. The strain data are organized by distance from the injection site. Colors match those of the markers shown in **a**. **d.** Same as **b**, but for the injection conducted at $\tau_0/\tau_p = 0.6$ with a constant pressure rate of $c = 15$ MPa/s. **e.** Same as **c**, but for the injection conducted at $\tau_0/\tau_p = 0.6$ with a constant pressure rate of $c = 15$ MPa/s.

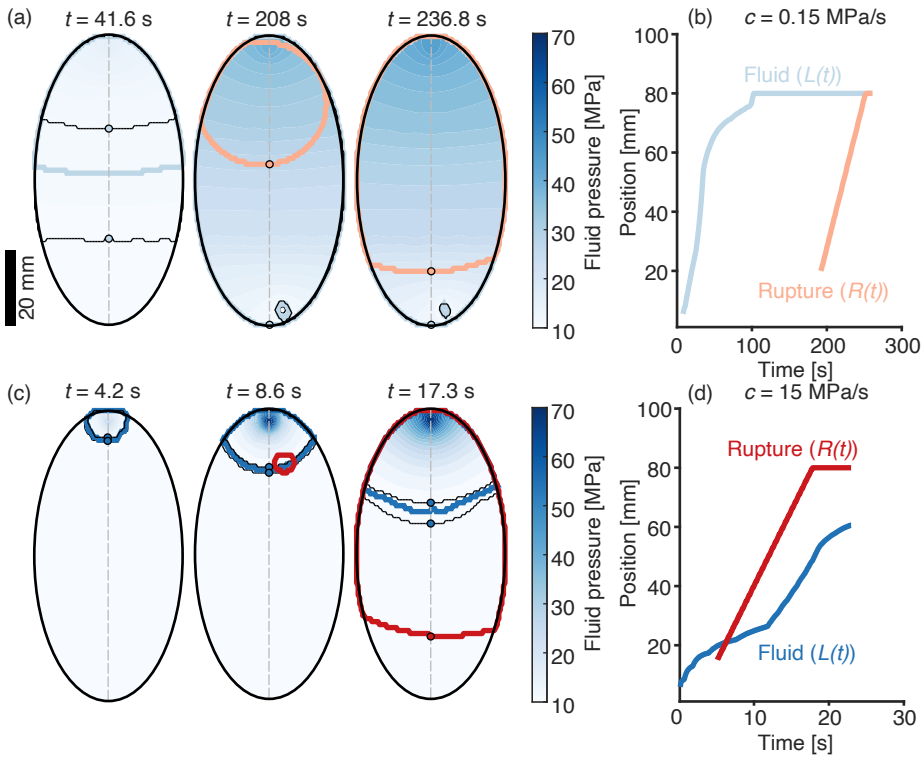

Figure 2. Inversion of R and L during fluid injection. a. Snapshots at three different times showing the propagation of the fluid pressure front L (in blue) and the slip front R (in red) during an injection performed at $\tau_0/\tau_p = 0.6$, with a constant pressure rate of $c = 0.15$ MPa/s. The color scales for R and L are the same as in Figure 3, and correspond to the value of c. The thin solid black lines indicate the position of the fluid pressure front for thresholds of 10.7 and 11.3 MPa, and L (blue) for 11 MPa. Colored circles correspond to the location of R (red) and L (blue) in the length of the fault (dashed line).**b.** Position of the front $R(t)$ and $L(t)$ along the length of the fault during the injection conducted at at $\tau_0/\tau_p = 0.6$, with a constant pressure rate of $c = 0.15$ MPa/s. **c.** Same as **a**, but for an injection conducted at $\tau_0/\tau_p = 0.6$ with a constant pressure rate of $c = 15$ MPa/s. **d.** Same as **b**, but for an injection conducted at $\tau_0/\tau_p = 0.6$ with a constant pressure rate of $c = 15$ MPa/s.

The minimization process yielded the optimal solution for the spatiotemporal evolution of fluid pressure during each injection (Extended Data S3). To track the propagation of the fluid pressure front along the fault, we applied a pressure threshold of 1 MPa larger than the initial fluid pressure along the fault. The interaction between the advancing slip front and the fluid pressure front is presented in Figure 2 for two distinct injection scenarios conducted at 60% of the fault's peak strength, with injection rates of 0.15 MPa/s and 15 MPa/s.

At the lower injection rate (Figures 2a and b), the fluid pressure front propagates throughout the entire fault before the initiation of slip front propagation. Once initiated, the slip front advances at a slow velocity of 0.6 mm/s, and eventually catches up with the fluid pressure front, doing so around 244 seconds after injection onset. At the higher injection rate (Figures 2c and d), the fluid pressure front also propagates first. However, at the onset of slip front propagation, L remains localized near the injection site. At this stage, R propagates at a faster velocity than L ($\dot{R} = 5$ mm/s), and overtakes it at $t = 8.56$ seconds (Figure 2b). These results confirm that an increase in the injection rate facilitates the transition between the two end-member cases: (i) a slip front $R(t)$ propagating behind the fluid pressure front $L(t)$, and (ii) a slip front $R(t)$ initially lagging behind the fluid pressure front $L(t)$ but eventually outpacing it, propagating ahead of it in the later stages (Figure 2b).

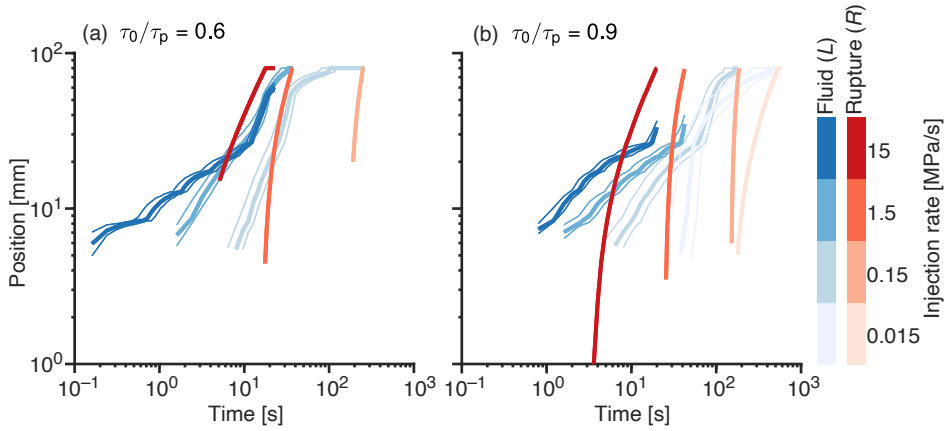

Figure 3. 1-D propagation of rupture $R(t)$ and fluid pressure $L(t)$. **a.** Evolution of the rupture dimension (red) and fluid front position (blue) along the fault length (Figure 2) as a function of time for injections conducted at $\tau_0/\tau_p = 0.6$. $L(t)$ represents the location of the fluid front for taken as 1 MPa above the initial, uniform pressure field (solid lines), $\pm$ 0.3 MPa (thin lines). The red and blue color scales correspond to the values of pressurisation rate c used in each injection. **b.** Same as **a**, but for injections conducted at $\tau_0/\tau_p = 0.9$.

Influence of initial stress and pressurisation rate on the fluid-driven slip front

We now compare the temporal evolution of both the slip front, $R(t)$, and the fluid pressure front, $L(t)$, along the long axis of the experimental elliptical fault (Figure 2) for: (i) the two initial stress states tested ($\tau_0/\tau_p = 0.6$ and $\tau_0/\tau_p = 0.9$, respectively), and (ii) each applied pressure rate c ranging from 0.015 to 15 MPa/s.

Our experimental results indicate that, regardless of the initial stress state, increasing c accelerates the propagation of both the fluid pressure front and the slip front (Figure 3). However, the initial stress state influences the transition between the two end-member cases previously discussed. At $\tau_0/\tau_p = 0.6$, only the injection conducted at $c = 15$ MPa/s allows $R(t)$ to outpace $L(t)$, at $t \approx 6$ (Figure 3a). In contrast, at $\tau_0/\tau_p = 0.9$, $R(t)$ outgrowths $L(t)$ for injections conducted at both $c = 1.5$ MPa/s and $c = 15$ MPa/s, at $t \approx 26$ and at $t \approx 5$ s, respectively (Figure 3b).

These observations are broadly consistent with theoretical expectations, as both τ_0 and c are expected to contribute to variations in the loading parameter[10,12], defined as:

$$T = \frac{1 - \tau_0/(f\sigma_0')}{\Delta p^*/\sigma_0'} \tag{1}$$

where f is the static friction of the fault, σ_0' is the initial effective normal stress along the fault, and Δp^* represents a characteristic pressure perturbation at the injection site. In our experiments, the appropriate characteristic pressure is $\Delta p^* = ca^2/\alpha$, where a is the injection borehole radius and α is the fault hydraulic diffusivity (see Methods). Equation 1

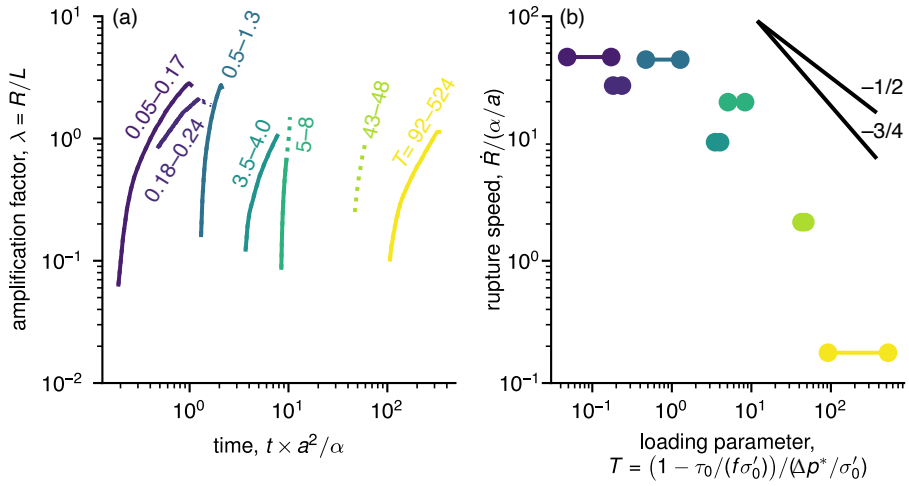

Figure 4. Influence of loading parameter T on slip and fluid propagation. a. Ratio $\lambda = R(t)/L(t)$ as a function of scaled time for all injections. The colored circles in transparency represent the complete evolution of λ, even after $L(t)$ or $R(t)$ have reached the bottom edge of the fault. The colored solid lines show the evolution of λ only during the period when both $L(t)$ and $R(t)$ are still propagating. **b.** Scaled rupture speed as a function of the loading parameter T.

highlights that an increase in both τ_0 or c, individually or together, leads to a decrease in T, which is expected to control the transition from the case $R \ll L$, termed "marginally pressurised fault", to the case $R \gg L$, termed "critically stressed fault"[10,12,34,35].

In our experiments, there is some uncertainty in the quantification of T, since we only have an imperfect knowledge of the friction coefficient, which is assumed constant in the theory of[12]. In practice, f is not constant but depends on slip rate and past history of the fault "state"[36,37]. Here, we estimate T using either a constant friction coefficient equal to 0.67, obtained independently based on measurements of τ_p, or by taking it equal to the normalised time $t \times \alpha/a^2$ at the initiation of rupture (see Methods, Equation 22). We also use our measurements of R and L to determine the time history of the amplification factor defined by $\lambda = R/L$. In contrast with injection scenarios at constant injected volume rate, where λ is fully determined by T and both R and L grow as $\sqrt{t}$[10,12,35], we anticipate that λ depends on both T and time in the case of injection at constant pressurisation rate (see Methods and Figure S4).

We indeed observe that experiments conducted at large T (low stress or low injection rate) tend to produce ruptures that start late and remain initially behind the fluid migration, whereas at low T the rupture rapidly outpaces the fluid (Figure 4a), in qualitative agreement with model results. The slip front typically nucleates within the pressurised area (Extended Data S2a), so that the initial values of λ are smaller than 1. With ongoing time, λ increases, which indicates that the slip front propagates faster than the pressure front. For the lowest values of T, λ eventually surpasses 1. Importantly, our results highlight that λ becomes larger than 1 at shorter timescale with decreasing the value of T, in agreement with numerical results (Extended Data S4). These results suggest that the larger the injection rate and the initial shear stress along the fault, and the faster R will outgrow L.

There are discrepancies between model and data that are due to the finite experimental system: in particular, at low pressure rates (i.e., large values of T), the slip front initiates in most of the cases after L already reached the opposite edge of the fault. For these cases, the corresponding λ values are not representative and are therefore biased due to the finite length of our experimental faults, which limit the propagation of both fronts in space (Figure 4a).

In addition, we observe a strong correlation between the slip front propagation velocity $\dot{R}$ and the loading parameter T (Figure 4b). Using our simplified model, we estimated $\dot{R}$ as a function of T throughout the entire injection duration. Our numerical simulations indicate that the rupture velocity is expected to slightly decrease over time (after an initial phase that depends on T), but tends to stabilise to nearly constant velocity at large time, consistent with our experimental observations (Figure 3, Extended Data S2). Furthermore, both our numerical and experimental results suggest that $\dot{R}$ scales with T^{-m}, with m ranging from $-3/4$ to $-1/2$ (Figure 4b and S5b). This scaling indicates that in critically stressed faults, slip fronts will nucleate earlier and propagate more rapidly as T decreases. This result is consistent with previous laboratory experiments which showed that high fluid injection rates promote early nucleation of dynamic slip along faults in polymer[38] and rocks[39].

Aseismic slip propagating further than fluid pressure during injection was previously inferred indirectly from field data[10]. Our results provide direct confirmation of this phenomenon in a crustal rock tested under upper crustal conditions (initial

effective pressure equivalent to that at 2 to 3 km depth). Our experiments also show that rupture growth is primarily controlled by a loading parameter that combines information about the initial stress, fault strength and injection rate, in agreement with simple models based on fracture mechanics[10,12]. Under our tested conditions, the slip front does not propagate as $\sqrt{t}$, but rather at a nearly constant velocity, in agreement with our model predictions. More generally, fracture mechanics models[12,40] (see Methods) imply that the propagation rate of the slip front is indicative of the injection scenario (constant volume rate, pressure or pressure rate), which may explain field studies reporting seismicity migration (natural or induced) that differ from the conventionally assumed square-root time dependence[7,8].

In nature, the occurrence of seismicity in response to fluid injection, even for small pressure change compared to hydrostatic values, indicates that faults are critically stressed, i.e., at a background stress close to the frictional strength[41,42], at least in intraplate regions. Therefore, we anticipate that the loading parameter T is small and faults should be prone to rapid propagation of aseismic slip beyond the pressurised region. However, in such cases, the predictive power of simple models based on constant friction and constant hydraulic properties might reach its limit, since strength perturbations due to rate-and-state effects[36,37] and variations in hydraulic properties due to stress changes and slip accumulation[27] can become substantial. Our experiment illustrate such limits: we only have approximate constraints on the value of T, and we detected time- and space-dependent variations in hydraulic diffusivity (Figure S3). More elaborate models that include some of these effects, such as rate-and-state friction, have been developed[11,43], but remain to be tested under realistic crustal conditions.

References

1. Heinicke, J. *et al.* Hydrothermal alteration as a trigger mechanism for earthquake swarms: the vogtland/nw bohemia region as a case study. *Geophys. J. Int.* **178**, 1–13 (2009).
2. Holtkamp, S. & Brudzinski, M. Earthquake swarms in circum-pacific subduction zones. *Earth Planet. Sci. Lett.* **305**, 215–225 (2011).
3. Chen, X., Shearer, P. & Abercrombie, R. Spatial migration of earthquakes within seismic clusters in southern california: Evidence for fluid diffusion. *J. Geophys. Res. Solid Earth* **117** (2012).
4. Duverger, C., Godano, M., Bernard, P., Lyon-Caen, H. & Lambotte, S. The 2003–2004 seismic swarm in the western corinth rift: Evidence for a multiscale pore pressure diffusion process along a permeable fault system. *Geophys. Res. Lett.* **42**, 7374–7382 (2015).
5. De Barros, L., Cappa, F., Deschamps, A. & Dublanchet, P. Imbricated aseismic slip and fluid diffusion drive a seismic swarm in the corinth gulf, greece. *Geophys. Res. Lett.* **47**, e2020GL087142 (2020).
6. Ross, Z. E., Cochran, E. S., Trugman, D. T. & Smith, J. D. 3d fault architecture controls the dynamism of earthquake swarms. *Science* **368**, 1357–1361 (2020).
7. Goebel, T. H. & Brodsky, E. E. The spatial footprint of injection wells in a global compilation of induced earthquake sequences. *Science* **361**, 899–904 (2018).
8. Dublanchet, P. & De Barros, L. Dual seismic migration velocities in seismic swarms. *Geophys. Res. Lett.* **48**, e2020GL090025 (2021).
9. Danré, P., Garagash, D., De Barros, L., Cappa, F. & Ampuero, J.-p. Control of seismicity migration in earthquake swarms by injected fluid volume and aseismic crack propagation. *J. Geophys. Res. Solid Earth* **129**, e2023JB027276 (2024).
10. Bhattacharya, P. & Viesca, R. C. Fluid-induced aseismic fault slip outpaces pore-fluid migration. *Science* **364**, 464–468 (2019).
11. Dublanchet, P. Fluid driven shear cracks on a strengthening rate-and-state frictional fault. *J. Mech. Phys. Solids* **132**, 103672 (2019).
12. Sáez, A., Lecampion, B., Bhattacharya, P. & Viesca, R. C. Three-dimensional fluid-driven stable frictional ruptures. *J. Mech. Phys. Solids* **160**, 104754 (2022).
13. Cebry, S. B. L. & McLaskey, G. C. Seismic swarms produced by rapid fluid injection into a low permeability laboratory fault. *Earth Planet. Sci. Lett.* **557**, 116726 (2021).
14. Passelègue, F. X., Brantut, N. & Mitchell, T. M. Fault reactivation by fluid injection: Controls from stress state and injection rate. *Geophys. Res. Lett.* **45**, 12–837 (2018).
15. Ye, Z. & Ghassemi, A. Injection-induced shear slip and permeability enhancement in granite fractures. *J. Geophys. Res. Solid Earth* **123**, 9009–9032 (2018).
16. Passelègue, F. X. *et al.* Initial effective stress controls the nature of earthquakes. *Nat. communications* **11**, 5132 (2020).

17. Ellsworth, W. L. Injection-induced earthquakes. *Science* **341**, 1225942 (2013).

18. Shapiro, S. A. *Fluid-induced seismicity* (Cambridge University Press, 2015).

19. Keranen, K. M. & Weingarten, M. Induced seismicity. *Annu. Rev. Earth Planet. Sci.* **46**, 149–174 (2018).

20. Kwiatek, G. *et al.* Controlling fluid-induced seismicity during a 6.1-km-deep geothermal stimulation in finland. *Sci. Adv.* **5**, eaav7224 (2019).

21. Shapiro, S. A., Huenges, E. & Borm, G. Estimating the crust permeability from fluid-injection-induced seismic emission at the ktb site. *Geophys. J. Int.* **131**, F15–F18 (1997).

22. Keranen, K. M., Savage, H. M., Abers, G. A. & Cochran, E. S. Potentially induced earthquakes in oklahoma, usa: Links between wastewater injection and the 2011 mw 5.7 earthquake sequence. *Geology* **41**, 699–702 (2013).

23. Sáez, A., Passelègue, F. & Lecampion, B. Maximum size and magnitude of injection-induced slow slip events. *Sci. Adv.* **11**, eadq0662 (2025).

24. McGarr, A. Maximum magnitude earthquakes induced by fluid injection. *J. Geophys. Res. solid earth* **119**, 1008–1019 (2014).

25. Galis, M., Ampuero, J. P., Mai, P. M. & Cappa, F. Induced seismicity provides insight into why earthquake ruptures stop. *Sci. advances* **3**, eaap7528 (2017).

26. Wibberley, C. A. & Shimamoto, T. Internal structure and permeability of major strike-slip fault zones: the median tectonic line in mie prefecture, southwest japan. *J. Struct. Geol.* **25**, 59–78 (2003).

27. Rutter, E. & Hackston, A. On the effective stress law for rock-on-rock frictional sliding, and fault slip triggered by means of fluid injection. *Phil. Trans. R. Soc. A* **375**, 20160001 (2017).

28. Cebry, S., Ke, C.-Y. & McLaskey, G. The role of background stress state in fluid-induced aseismic slip and dynamic rupture on a 3-m laboratory fault. *J. Geophys. Res. Solid Earth* **127**, e2022JB024371 (2022).

29. Guglielmi, Y., Cappa, F., Avouac, J.-P., Henry, P. & Elsworth, D. Seismicity triggered by fluid injection–induced aseismic slip. *Science* **348**, 1224–1226 (2015).

30. Cappa, F., Scuderi, M. M., Collettini, C., Guglielmi, Y. & Avouac, J.-P. Stabilization of fault slip by fluid injection in the laboratory and in situ. *Sci. advances* **5**, eaau4065 (2019).

31. Brantut, N. Dilatancy-induced fluid pressure drop during dynamic rupture: Direct experimental evidence and consequences for earthquake dynamics. *Earth Planet. Sci. Lett.* **538**, 116179 (2020).

32. Brantut, N. & Aben, F. M. Fluid pressure heterogeneity during fluid flow in rocks: new laboratory measurement device and method. *Geophys. J. Int.* **225**, 968–983 (2021).

33. Dublanchet, P. *et al.* Kinematic inversion of aseismic fault slip during the nucleation of laboratory earthquakes. *J. Geophys. Res. Solid Earth* **129**, e2024JB028733 (2024).

34. Garagash, D. I. & Germanovich, L. N. Nucleation and arrest of dynamic slip on a pressurized fault. *J. Geophys. Res. Solid Earth* **117** (2012).

35. Viesca, R. C. Self-similar fault slip in response to fluid injection. *J. Fluid Mech.* **928**, A29 (2021).

36. Scholz, C. H. Earthquakes and friction laws. *Nature* **391**, 37–42 (1998).

37. Marone, C. Laboratory-derived friction laws and their application to seismic faulting. *Annu. Rev. Earth Planet. Sci.* **26**, 643–696 (1998).

38. Gori, M., Rubino, V., Rosakis, A. J. & Lapusta, N. Dynamic rupture initiation and propagation in a fluid-injection laboratory setup with diagnostics across multiple temporal scales. *Proc. Natl. Acad. Sci.* **118**, e2023433118 (2021).

39. Ji, Y., Wang, L., Hofmann, H., Kwiatek, G. & Dresen, G. High-rate fluid injection reduces the nucleation length of laboratory earthquakes on critically stressed faults in granite. *Geophys. Res. Lett.* **49**, e2022GL100418 (2022).

40. Saez, A. A. *Three-dimensional fluid-driven frictional ruptures: theory and applications*. Ph.D. thesis, École Polytechnique Fédérale de Lausanne (2023).

41. Zoback, M. D. & Harjes, H.-P. Injection-induced earthquakes and crustal stress at 9 km depth at the ktb deep drilling site, germany. *J. Geophys. Res. Solid Earth* **102**, 18477–18491 (1997).

42. Zoback, M. D., Townend, J. & Grollimund, B. Steady-state failure equilibrium and deformation of intraplate lithosphere. *Int. Geol. Rev.* **44**, 383–401 (2002).

43. Garagash, D. I. Fracture mechanics of rate-and-state faults and fluid injection induced slip. *Philos. Transactions Royal Soc. A* **379**, 20200129 (2021).

44. Eccles, D., Sammonds, P. & Clint, O. Laboratory studies of electrical potential during rock failure. *Int. J. Rock Mech. Min. Sci.* **42**, 933–949 (2005).

45. Jaeger, J. C., Cook, N. G. & Zimmerman, R. *Fundamentals of rock mechanics* (John Wiley & Sons, 2009).

46. Almakari, M., Chauris, H., Passelègue, F., Dublanchet, P. & Gesret, A. Fault's hydraulic diffusivity enhancement during injection induced fault reactivation: application of pore pressure diffusion inversions to laboratory injection experiments. *Geophys. J. Int.* **223**, 2117–2132 (2020).

47. Plessix, R.-E. A review of the adjoint-state method for computing the gradient of a functional with geophysical applications. *Geophys. J. Int.* **167**, 495–503 (2006).

48. Carslaw, H. & Jaeger, J. *Heat in solids*, vol. 19591 (Clarendon Press, Oxford, 1959).

Methods

Experimental methods

The material used was Lanhélin granite, a coarse-grained granite from Brittany, France. Intact Lanhélin granite has a very low permeability (lower than 10^{-21} m^2, which is the resolution of our equipment), and is considered impermeable over the timescale of our experiments. A cylindrical sample of 40 mm in diameter was cored and precisely ground to a length of 100 mm. The cylinder was then saw-cut at a 30° angle relative to its axis of revolution, creating an elliptical fault surface measuring 40 mm in width and 80 mm in length along strike. This surface was subsequently prepared using a surface grinder. Two 2 mm diameter boreholes were drilled from both sides of the sample, passing through the material and intersecting the fault surface. The center of the boreholes were offset 4-5 mm from the sample's edge to maximize the fluid diffusion path along the fault. The prepared, faulted sample was then enclosed in a Viton jacket and instrumented with 8 strain gauges and 3 additional pore pressure transducers[31,32], as schematically shown in Figure 1a. The pore pressure sensors have a contact diameter of 7 mm with the sample surface, and were placed across the fault to ensure good hydraulic connection between the fault zone and the sensors dead volume. The instrumented sample was placed in the triaxial oil-medium apparatus at the Rock and Ice Physics Laboratory, University College London[44]. The borehole at the upstream end of the sample was connected to a high-capacity servo-hydraulic pore fluid intensifier equipped with a pressure transducer and a linear variable differential transformer (LVDT) to monitor fluid volume changes. The borehole bottom end was sealed and connected to a closed reservoir with its own pressure transducer. Distilled water was used as the pore fluid.

Confining pressure and axial differential stress were independently controlled by an electromechanical pump and a servo-hydraulic actuator, respectively. Axial shortening was measured by external LVDTs, corrected for the stiffness of the loading column. Load was measured with an external load cell and corrected for seal friction. Differential stress was calculated as the corrected load divided by the sample's cross-sectional area. Fault slip was estimated by projecting the corrected axial shortening onto the fault plane, and average normal and shear stresses on the fault were computed by resolving the triaxial stress state onto the inclined fault surface[45].

The pore pressure sensors were calibrated using the method detailed in[32], by imposing a set a constant, uniform confining and pore pressures and determining linear regression coefficients between output voltages and confining and pore pressure. From these coefficients, the local pore pressure at each sensor location was determined from the measured voltage and known confining pressure.

All mechanical data including load cell, pore pressure measurements, LVDT, and strain gauges were recorded during the entire experiments at a sampling rate of 1 Hz. Additionally, the strain gauges, the pore pressure at the five locations and one external LVDT were recorded during each injection at a sampling rate of 20 kHz.

Experiments were conducted at a confining pressure of 80 MPa, with an initial pore pressure of 10 MPa. To determine the shear stress at fault slip onset (τ_p) under constant pore pressure, an axial loading test was performed. The load was then reduced to a predetermined initial stress (τ_0), after which the actuator position was held constant using the servo-controlled feedback loop based on external displacement sensors. This setup constituted a "stress relaxation" test[14,15,27], where elastic strain energy was stored in the loading column. Fault reactivation initiated the release of this stored energy through sample shortening via fault slip. Slip events were accompanied by a proportional reduction in applied stress, governed by the machine stiffness. This method ensured controlled fault slip, limiting runaway failure while still allowing for stick-slip behavior.

Synthetic crack propagation using finite element modeling

To test the robustness of what we identified as the passage of the slip front on the strain gauges, we modeled the axial strain at the gauge locations that would arise from the propagation of a synthetic crack on the fault, following the FEM Green's

function approach presented in[33]. Green's function relating slip on the fault and strain at gauges locations are first computed from the static equilibrium of one half of the sample, assuming experimental boundary conditions (no displacement at the bottom, constant confining pressure of 70 MPa on lateral boundaries), and unit slip on the fault surface. Then we consider a slip distribution δ corresponding to a circular crack growing from the injection site center with constant rupture speed $\dot{R}$ and stress drop $\Delta\tau$. δ is convolved with Green's functions to compute axial strains at gauges locations during the propagation of the simulated rupture. Our numerical results highlight that the first abrupt strain release recorded at the strain gauge location is consistent with the passage of the slip front (Figure S1).

Inversion of the slip front velocity

For each injection, the first abrupt strain release recorded on each strain gauge was manually picked. The rupture initiation point and rupture velocity were then estimated using a least squares inversion method by comparing the experimental arrival times with theoretical arrival times calculated as follows.

The forward problem is modeled using a simplified assumption that the rupture front is circular. The theoretical arrival time at strain gauge i, denoted t_i, is given by

$$t_i = t_0 + \frac{\sqrt{(x-x_i)^2+(y-y_i)^2}}{\dot{R}}, \tag{2}$$

where t_0 is the rupture origin time, (x,y) are the coordinates of the rupture initiation point on the fault plane, $\dot{R}$ is the rupture velocity, and (x_i,y_i) are the coordinates of the strain gauge.

The inverse problem involves determining the model parameters x, y, t_0, and $\dot{R}$. To solve this, we employed a grid-search approach, systematically exploring a range of possible values for each parameter and evaluating a likelihood function based on the least squares criterion:

$$\min_{x,y,t_0} \sum_{i=1}^{N} \left(t_i^{\exp} - t_0 - \frac{\sqrt{(x-x_i)^2+(y-y_i)^2}}{\dot{R}} \right)^2 \tag{3}$$

where $t_i^{\exp}$ are the experimentally measured arrival times, and N is the total number of observations.

Inversion of the fluid pressure along the fault

Based on previous study[46], we developed an inversion procedure to estimate the time- and space-dependent hydraulic diffusivity $D(\mathbf{x},t)$ along the experimental fault from sparse pressure observations. The two main elements are the parametrization of D and the way to update D to fit the observed data at the transducer locations. We first recall the forward problem (diffusion equation) and the objective function. We then discuss the parametrization and finally provide an expression for the gradient, indicating how to iteratively update D.

Forward modeling

The spatio-temporal evolution of fluid pressure p is modeled by the diffusion equation:

$$\frac{\partial p}{\partial t}(\mathbf{x},t) = \nabla \cdot (D(\mathbf{x},t)\,\nabla p)\,. \tag{4}$$

We applied Neumann condition at the domain boundary: $\partial_n p = 0$, and Dirichlet condition at source locations: $p(\mathbf{x_s},t) = p_s(t)$, where $\mathbf{x_s}$ denotes the source positions, corresponding to the two boreholes along the fault (Figure 1a) and p_s the imposed pressure. To account for dead-volume effects in the downstream pore pressure system, we constrained the inversion by imposing the fluid pressure at the injection site (P_1) as well as the pore pressure measured in the second borehole (P_5).

The diffusion equation is solved with an explicit time-stepping scheme and a finite element method suited with a mesh description of the pressure.

Objective function

We aim to find the optimal diffusivity field $D(\mathbf{x},t)$ such that the simulated pressure $p(\mathbf{x}_r,t)$ (depending on D) matches the observed data $p^{\text{obs}}(\mathbf{x}_r,t)$ at pore pressure transducer locations $\mathbf{x}_r$, by minimizing the least-squares misfit functional:

$$J[D(\mathbf{x},t)] = \frac{1}{2} \iint dt\, d\mathbf{x}_r \left| p(\mathbf{x}_r,t) - p^{\text{obs}}(\mathbf{x}_r,t) \right|^2. \tag{5}$$

Before explaining how to optimize the objective function, we first discuss the D parametrization.

D parametrization

As only sparse pore pressure transducers are available, it is essential to constrain the inversion with a suitable parameterization for $D(\mathbf{x},t)$. Instead of looking for values at each spatial positions $\mathbf{x}$ and time coordinates t, that would not be well constrained by the data, the diffusivity field is parameterized using a spatial basis functions $B_i(\mathbf{x})$:

$$D(\mathbf{x},t) = \sum_{i=1}^{N} D_i(t) B_i(\mathbf{x}), \tag{6}$$

where $D_i(t)$ are the time-dependent weights to be inverted. Based on the acquisition geometry, we assume three independent regions ($N = 3$), each monitored by an individual fluid pressure transducer (P_2, P_3, and P_4), within which $D(\mathbf{x},t)$ is assumed homogeneous in space. Thus $B_i(\mathbf{x})$ is simply 1 in region i and 0 in other regions.

The reconstruction from D_i to $D(\mathbf{x},t)$ is simply given by Equation 6. The decomposition from $D(\mathbf{x},t)$ to D_i is obtained by minimizing the differences $\sum_{i=1}^{N} D_i t) B_i(\mathbf{x}) - D(\mathbf{x},t)$ in a least-squares sense. For each time t, it consists in solving a linear system:

$$\sum_{i=1}^{N} \langle B_k, B_i \rangle_x D_i(t) = \langle B_k, D(\mathbf{x},t) \rangle_{\mathbf{x}} \tag{7}$$

where $\langle , \rangle_{\mathbf{x}}$ denotes the scalar product and k ranges from 1 to N.

Finally, to allow for variations in diffusivity across several orders of magnitude, we define the logarithmic variable $D_i^{\mathrm{L}}(t) = \log\left(D_i(t)/D_r\right)$, so that $D_i(t) = D_r \exp D_i^{\mathrm{L}}(t)$. D_r is a fixed diffusivity value. We thus aim at determining $D_i^{\mathrm{L}}(t)$ for the three regions i and for all times t.

Gradient derivation

The derivative of J with respect to $D_i^{\mathrm{L}}(t)$ is given as

$$\frac{\partial J}{\partial D_i^{\mathrm{L}}(t)} = \frac{\partial D_i(t)}{\partial D_i^{\mathrm{L}}(t)} \left\langle \frac{\partial D(\mathbf{x},t)}{\partial D_i(t)}, \frac{\partial J}{\partial D(\mathbf{x},t)} \right\rangle_{\mathbf{x}}. \tag{8}$$

By definition of $D_i^{\mathrm{L}}(t)$, the first term reads $\partial D_i(t)/\partial D_i^{\mathrm{L}}(t) = D_r \exp D_i^{\mathrm{L}}(t) = D_i(t)$, while the second is simply $\partial D(\mathbf{x},t)/\partial D_i(t) = B_i(\mathbf{x})$. The last term is more complex and can be obtained with the adjoint-state method[47], as:

$$\frac{\partial J}{\partial D(\mathbf{x},t)} = \nabla p(\mathbf{x},t) \cdot \nabla \lambda_{\mathrm{p}}(\mathbf{x},t), \tag{9}$$

where the adjoint pressure $\lambda_{\mathrm{p}}(\mathbf{x},t)$ satisties a similar diffusion equation as for the forward pressure $p(\mathbf{x},t)$:

$$\frac{\partial \lambda_{\mathrm{p}}}{\partial t}(\mathbf{x},t) = -\nabla \cdot \left(D(\mathbf{x},t) \nabla \lambda_{\mathrm{p}}\right) - \int d\mathbf{x_r} \delta(\mathbf{x} - \mathbf{x_r}) \left(p - p^{\mathrm{obs}}(\mathbf{x_r},t)\right). \tag{10}$$

The source term is zero, except for a spatial position at an observation transducer location. As for the forward pressure, zero-Neumann conditions are imposed to the adjoint pressure λ_{p}, but here λ_{p} is set to 0 at the injection location. The adjoint diffusion equation is as stable as the forward diffusion equation, as it is solved backwards, from the final time to the initial time. Combining the different expressions, the gradient reads

$$\frac{\partial J}{\partial D_i^{\mathrm{L}}(t)} = D_i(t) \int d\mathbf{x} B_i(\mathbf{x}) \nabla p(\mathbf{x},t) \cdot \nabla \lambda_{\mathrm{p}}(\mathbf{x},t). \tag{11}$$

The inversion is performed using a standard non-linear quasi-Newton (L-BFGS) algorithm. Results for diffusivity values and pore pressure fits are shown in Figure S3.

Fracture mechanics model

Our experimental setup closely resembles the theoretical model explored by[12], whereby a planar frictional fault embedded in an infinite elastic medium is loaded by an initially uniform background stress τ_0, and fluid injection is simulated by an on-fault pore pressure source at a point or in a small circular borehole of radius a. In our experiments, the sample is finite, but an infinite model should capture the early stages of slip nucleation and propagation. The loading parameter that controls the propagation of slip is given by

$$T = (1 - \tau_0/f\sigma_0')/(\Delta p^*/\sigma_0'), \tag{12}$$

where f is the friction coefficient on the fault (assumed constant), σ_0' is the effective normal stress applied on the fault, and Δp^* is a characteristic fluid pressure related to the injection.[12] treat two different injection scenarios: one where fluid is injected at constant volume rate, in which case Δp^* is given by a combination of the injection rate, fault diffusivity and fault compressibility, and one where fluid is injected at constant pressure, in which case Δp^* is simply the applied pore pressure at the borehole.

Here, we follow the steps of[12] and determine the solution for rupture size and fluid pressure in the case of injection at constant pressure rate, relevant to our experimental injection scenario.

The first step is to solve for the fluid pressure distribution along the the fault plane. Denoting $p(r,t)$ the fluid pressure as a function of radial position r (measured from the borehole center) and time t, the radial diffusion problem is written as

$$\frac{\partial^2 p}{\partial r^2} + \frac{1}{r}\frac{\partial p}{\partial r} = \frac{1}{\alpha}\frac{\partial^2 p}{\partial t^2}, \tag{13}$$

where α is the hydraulic diffusivity of the fault, assumed constant. The boundary condition at the well radius a is

$$p(a,t) = p_o + ct, \tag{14}$$

where p_0 is the initial (uniform) pore pressure and c is the constant pressurisation rate. The solution is of the form

$$p(r,t) = p_0 + \Delta p^* \Pi(r,t), \tag{15}$$

where $\Delta p^* = ct_{\text{diff}}$ is a characteristic pressure combining the injection rate c and the diffusion time around the well $t_{\text{diff}} = a^2/\alpha$, and $\Pi(r,t)$ is a nondimensional function that characterizes the spatio-temporal pore pressure distribution. That function can be expressed as the product

$$\Pi(r,t) = (t/t_{\text{diff}}) \times F(r/a, t/t_{\text{diff}}), \tag{16}$$

where $F(r/a,t/t_{\text{diff}})$ ranges from 1 at $r=a$ to 0 at $r \to \infty$. In practice, we compute $\Pi(r,t)$ by numerical inversion of the solution of (13) in the Laplace domain[48]. The solution for $p(r,t)$ provides us with the position $L(t)$ of the fluid pressure "front": although there is no well-defined "front" in a diffusion problem, we define $L(t)$ as the position r where pore pressure is $10^{-3}\Delta p^*$ above p_0. The factor 10^{-3} is arbitrary, but other definitions would offset $L(t)$ by some value while retaining the same qualitative features.

We determine how a circular rupture expands in response to the pore pressure field $p(r,t)$ by using the fracture mechanics criterion $K=0$, where K is the stress intensity factor at the rupture tip. This growth criterion assumes that the rupture is non singular, i.e., we neglect potential toughness terms arising from nonlinearities in the rupture cohesive zone. In terms of on-fault stresses, this criterion is expressed as[12]

$$\int_0^{R(t)} \frac{\Delta\tau(r,t)}{\sqrt{R(t)^2 - r^2}} r dr = 0, \tag{17}$$

where $R(t)$ is the rupture radius, and the stress drop is given by

$$\Delta\tau(r,t) = \tau_0 - f \times (\sigma_0' - \Delta p(r,t)). \tag{18}$$

Note that $\Delta p(r,t) = p(r,t) - p_0$ is equal to ct inside the well ($r \le a$). It is therefore obvious that there will be no rupture at all unless

$$ct \ge \sigma_0' - \tau_0/f. \tag{19}$$

Using the notation (16), the condition (17) is rewritten as

$$\frac{1}{\bar{R}} \int_0^{\bar{R}} \frac{F(r,t) r}{\sqrt{\bar{R}^2 - r^2}} dr = T/\bar{t}, \tag{20}$$

where we have defined normalised quantities $\bar{R} = R/a$ and $\bar{t} = t\alpha/a^2$, and the loading parameter

$$T = \frac{1 - \tau_0/(f\sigma_0')}{\Delta p^*/\sigma_0'}, \tag{21}$$

where again we recall that $\Delta p^* = ca^2/\alpha$. With this notation, the rupture initiation condition is expressed as

$$\bar{t} \geq T. \tag{22}$$

We solve numerically for R in Equation (20) as a function of T and time t. The results are shown in Figure S4(a), where we also show the fluid front position. For small T (large injection rate, dark red lines), the rupture front significantly outpaces the fluid pressure front. For large T (small injection rate, light red lines), the rupture front initiates only when sufficient pressure has been reached at the well (condition 22), and is initially behind the fluid pressure front.

By contrast with injection at constant volume rate, here the amplification factor $\lambda = R/L$ depends on both T and time (Figure S4b). In all cases, λ increases with increasing time. For large values of T (marginally pressurised faults, small injection rate), rupture initiates when L is already large, so λ is initially small (rupture front lagging behind fluid front). With increasing time, λ gradually increased and R eventually outpaces L. For small values of T (critically stress fault, large injection rate), R rapidly outgrows L.

The rupture growth velocity can be extracted from the model (Figure S5). Beyond the rupture initiation phase, for $\bar{t}$ much larger than T, the rupture velocity tends to decrease slightly with increasing time, whereas the fluid front velocity decreases more rapidly. There is a clear trend of larger rupture velocities at lower T, i.e., faster injection rates and/or higher background stress promote faster rupture growth (Figure S5b). Rupture velocity is found to scale with the loading parameter as $T^{-1/2}$ to $T^{-3/4}$, depending on injection time.

Acknowledgements

The authors thank Dmitry Garagash, Rob Viesca, Barnaby Fryer, Alexis Saez and Brice Lecampion for useful discussions. Financial support from the European Union Horizon 2020 research and innovation programme (grant agreements 804685 and 101088963 to NB, and 101041966 to FXP), the UK Natural Environment Research Council (grant NE/M016471/1 to NB) and from the Leverhulme Trust (Philip Leverhulme Prize to NB) is gratefully acknowledged.

Author contributions statement

F.X.P. and N.B. conceived the study, F.X.P. and N.B. conducted the experiment, F.X.P. analyzed the experimental data, N.B. developed the pore pressure transducers and the theoretical background, F.X.P. and P.D. analysed the results in the framework of inverse problems. H.C., P.D. and F.X.P. conceived the inversion procedure with the inputs of N.B., F.X.P. and N.B. wrote the first draft of the manuscript with the inputs of P.D. and H.C. All authors reviewed the manuscript.

Additional information

Competing interests The authors declare no competing interests.

Experiment	τ_0/τ_p [MPa]	P_c [MPa]	P_f [MPa]	c [MPa/sec]
phase 1	0.6	80	10	0.15
phase 2	0.6	80	10	1.5
phase 3	0.6	80	10	15
phase 4	0.9	80	10	0.015
phase 5	0.9	80	10	0.15
phase 6	0.9	80	10	1.5
phase 7	0.9	80	10	15

Supplementary Table S1. Summary of the initial state of stress and of the pressure rate imposed during the seven injections conducted in this study.

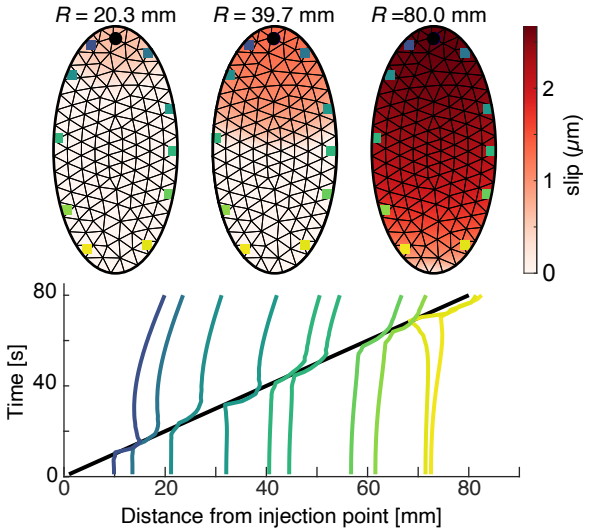

Supplementary Figure S1. Illustration of the synthetic rupture model with a circular expanding slip patch at constant rupture speed. Top: three snapshots of slip distribution for three rupture dimensions. Colored squares indicate positions where axial strain is computed from synthetic Green's functions. Bottom: Simulated axial strain records, plotted as a function of distance. from injection point (i.e., distance from rupture initiation point). The onset of strain decrease is a good indicator of the position of the slip front (black line).

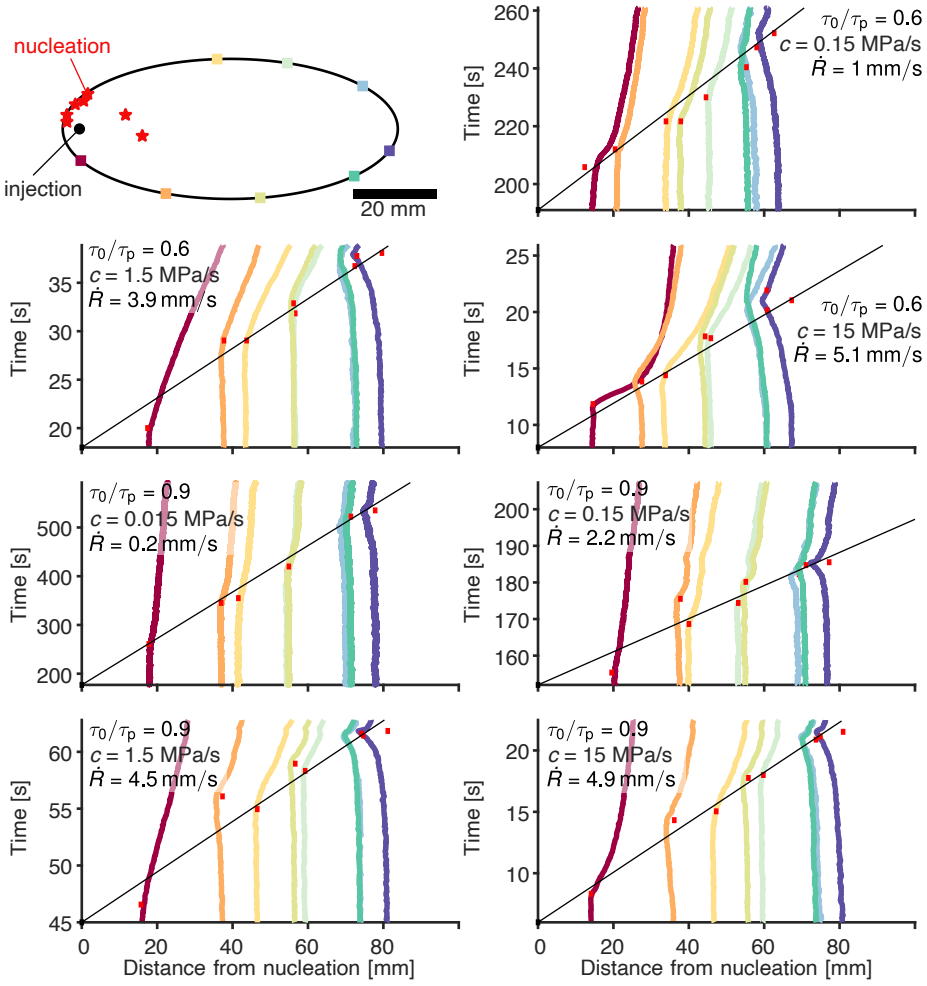

Supplementary Figure S2. Inversion of rupture-front velocity for all injection events. The first panel shows the inferred rupture initiation points and the locations of strain gauges (indicated by colored squares). The subsequent panels present the temporal evolution of strain recorded by each strain gauge positioned around the fault. The onset of strain drop at each gauge (marked by red squares) was used to invert for the rupture-front velocity. The best-fit rupture velocity, $\dot{R}$, is represented by the solid black line.

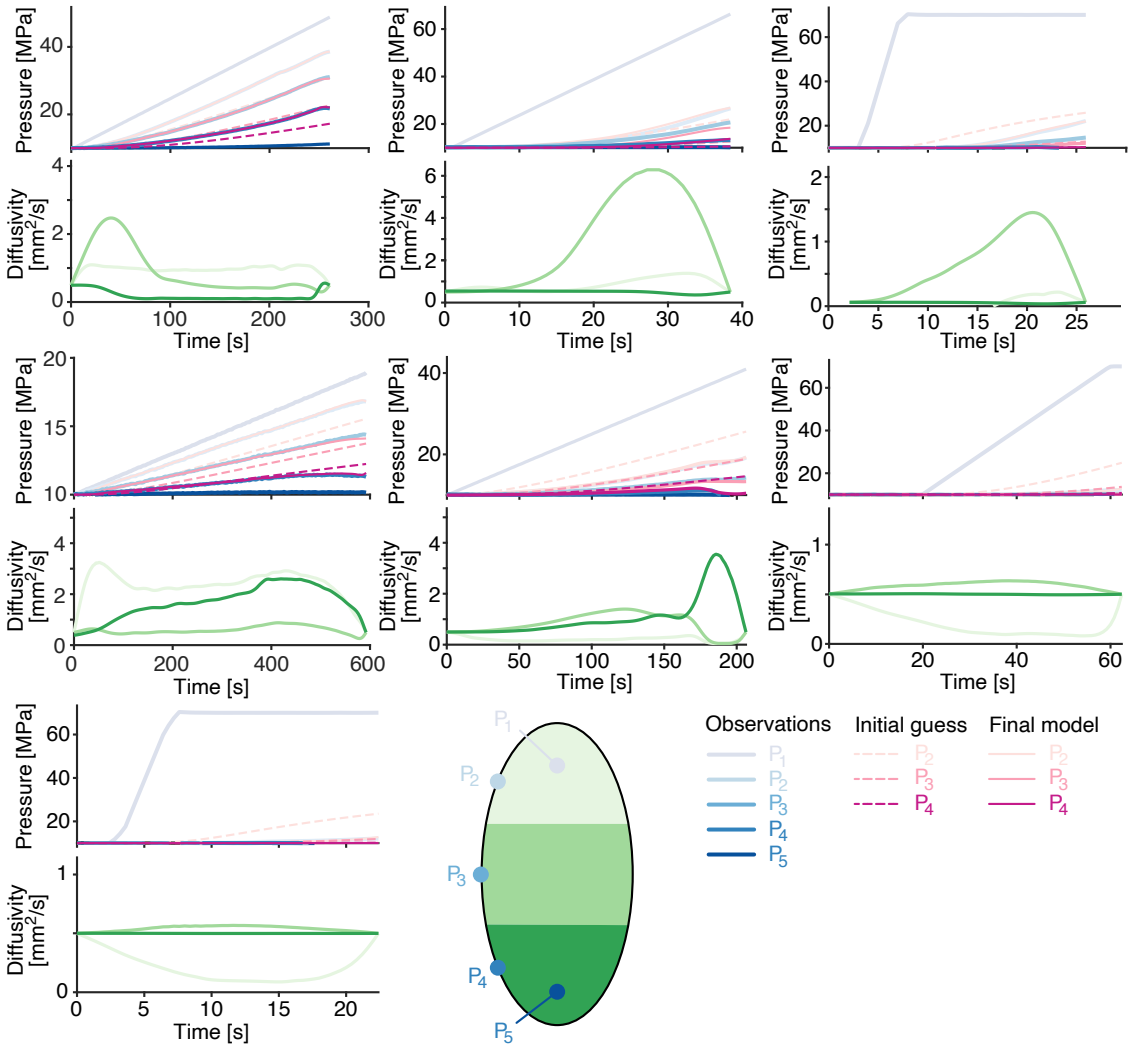

Supplementary Figure S3. Inversion of fault zone hydraulic diffusivity. Each pair of subplots displays the measured pore pressure data (blue lines), the initial model predictions assuming uniform diffusivity (dashed purple lines), and the final model predictions (solid purple lines) using inverted diffusivities for each fault regions (green curves). Experimental conditions are summarized in Table S1. The bottom-left panels show the locations of the pore pressure transducers and the corresponding fault regions over which hydraulic diffusivity was inverted as a function of time. Colored regions indicate the spatial domains associated with each transducer, corresponding to the curves shown in the adjacent subplots.

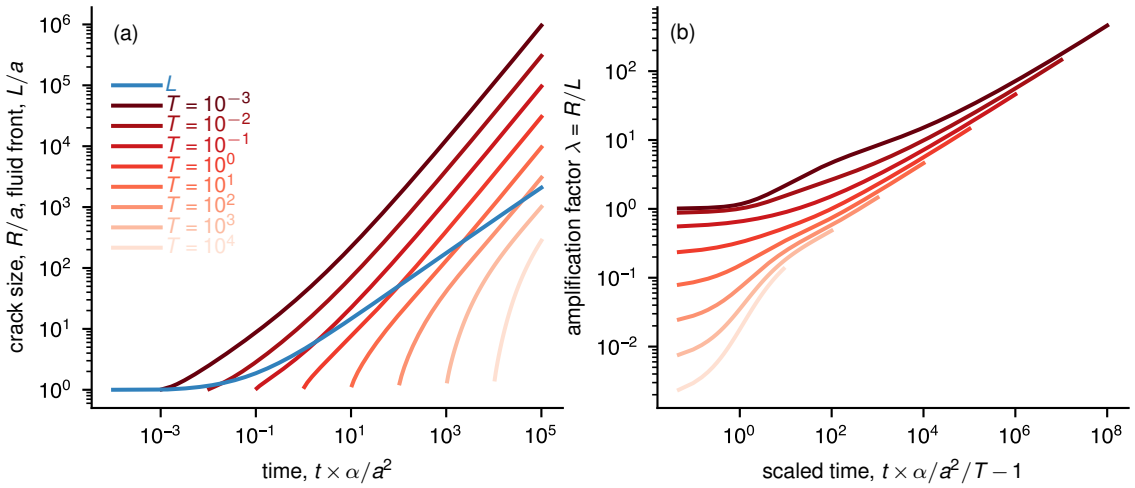

Supplementary Figure S4. Solution of rupture and fluid diffusion model for constant pressurisation rate (Equation 20). (a) Rupture front (red) and fluid front (blue) expansion as a function of normalised time, for a range of loading parameters T. Note that rupture initiates when $t\alpha/a^2$ becomes larger than T. (b) Amplification factor $\lambda = R/L$ as a function of rescaled time $t\alpha/a^2/T - 1$.

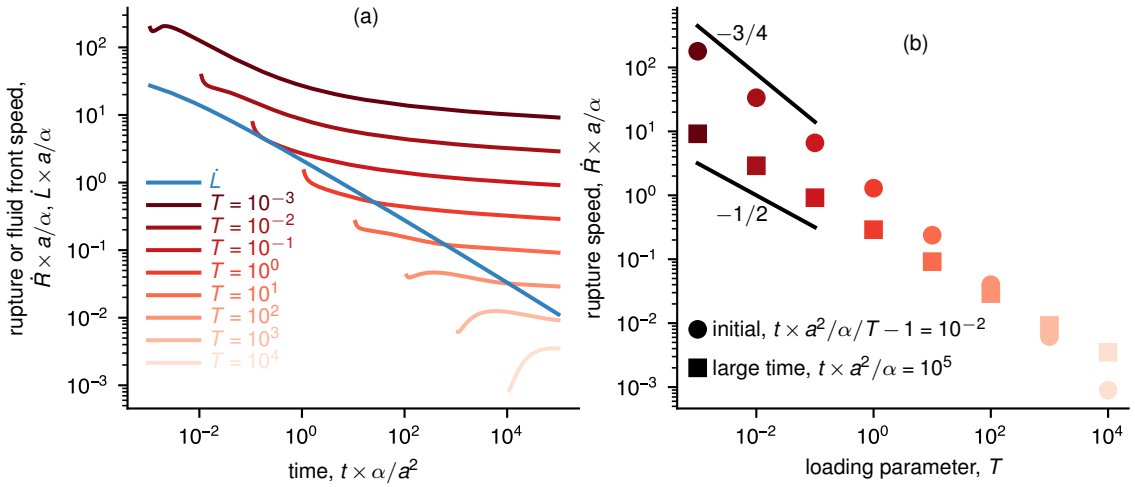

Supplementary Figure S5. Rupture and fluid migration speeds. (a) Rate of rupture (red) and fluid front (blue) propagation as a function of time. (b) Initial rupture speed (circles) and rupture speed at large time (squares) as a function of loading parameter.